FEBS Letters

FEBS PRESS science publishing by scientists

Ligand-dependent intra- and interdomain motions in the PDZ12 tandem regulate binding interfaces in postsynaptic density protein-95

Bertalan Kovács[1,2], Nóra Zajácz-Epresi[1] and Zoltán Gáspári[1]

1 Faculty of Information Technology and Bionics, Pázmány Péter Catholic University, Budapest, Hungary
2 3in Research Group, Faculty of Information Technology and Bionics, Pázmány Péter Catholic University, Esztergom, Hungary

Correspondence
Z. Gáspári, Pázmány Péter Catholic University, Faculty of Information Technology and Bionics, Prater str. 50/A, Budapest 1083, Hungary
Tel: +36 1 8864780
E-mail: gaspari.zoltan@itk.ppke.hu

(Received 13 June 2019, revised 10 September 2019, accepted 20 September 2019, available online 12 October 2019)

doi:10.1002/1873-3468.13626

Edited by Stuart Ferguson

[Correction added on 25 February 2020, after first online publication: The authors have noticed an inaccuracy in panel D of Fig. S9. At the end of the subsection "Dominant motions in the free form are redistributed by ligand binding in a domain specific way", the statement "On the other hand, internal motions in the complex form show poor overlap with those either of the free form or of the whole ensemble. Only the first two PCs of the free form overlap well with those of the whole ensembles (Fig. S9C,D). It can be stated, therefore, that in the complex form of PDZ2, new types of internal motions emerge that represent the bending of the β1-β2 loop in PC1, and of the β1-β2 and β2-β3 loops in PC2, but in a different direction." has been replaced with the text "The overlap between the internal motions of the whole ensemble and those of the free and complex states (Fig. S9C,D) also conform this observation." Figure S9 has also been replaced with the amended version.]

The postsynaptic density protein-95 (PSD-95) regulates synaptic plasticity through interactions mediated by its peptide-binding PDZ domains. The two N-terminal PDZ domains of PSD-95 form an autonomous structural unit, and their interdomain orientation and dynamics depend on ligand binding. To understand the mechanistic details of the effect of ligand binding, we generated conformational ensembles using available experimentally determined nuclear Overhauser effect interatomic distances and S^2 order parameters. In our approach, the fast dynamics of the two domains is treated independently. We find that intradomain structural changes induced by ligand binding modulate the probability of the occurrence of specific domain–domain orientations. Our results suggest that the β2-β3 loop in the PDZ domains is a key regulatory region, which influences both intradomain motions and supramodular rearrangement.

Keywords: molecular dynamics simulation; PDZ tandem; PSD-95; structural ensembles; supramodular dynamics

Abbreviations
DHR, discs-large homology region; eTCSPC, ensemble time correlated single photon counting; FRET, Förster resonance energy transfer; hPTP1E, human protein tyrosine phosphatase 1E; NMR, nuclear magnetic resonance; NOE, nuclear Overhauser effect; PCA, principal component analysis; PSD-95, postsynaptic density protein-95.

PDZ domains (PSD-95/Discs-large/ZO1), also known as discs-large homology region (DHR) or GLGF repeats for their conserved ligand-binding motif, are common protein-binding modules with about 270 copies occurring in 150 proteins in the human proteome [1,2]. While being involved in maintaining epithelial cell polarity, regulating signaling pathways, and establishing tight junctions in metazoans, their most widely studied role is organizing synaptic complexes by clustering membrane receptors and ion channels in the postsynaptic density [2–7].

The PDZ domain is often as regarded the glue that binds signaling complexes together in nerve cells. The PSD-95 (postsynaptic density protein 95, also referred to as SAP-90 or DLG4 by its encoding gene in humans), member of the MAGUK family (membrane-associated guanylate kinase), contains multiple PDZ domains, which allows it to function not only as a scaffold, but also as an adaptor protein to downstream intracellular signaling pathways [4,7–10]. Its abundance in the postsynaptic density and a number of interaction partners have made it a frequent research subject to understand signal transduction [10]. Because of its role in regulating synaptic plasticity, PSD-95 is implicated in several neurological disorders, like Alzheimer's disease or neuropathic pain, and its PDZ domains are favored drug targets [10,11].

The approximately 90-residue long PDZ domains contain 6 β-strands in a semiopen barrel-like formation, which is flanked by 2 α-helices (Fig. 1) [12,13]. The ligand-binding site recognizes short C-terminal peptide sequences, with the C-terminal hydrophobic residue being accommodated at the carboxylate-binding loop [4,6]. PDZ domains have traditionally been categorized into 3 classes based on the 4 C-terminal residues (-X-[S/T]-X-Φ, -X-Φ-X-Φ, and -X-[D/E]-X-Φ for classes I, II, and III, respectively, where Φ denotes a hydrophobic residue and X denotes any residue), but lately more complicated specificity trees were introduced that extend the binding pattern well beyond the identity of the −2 residue [1,5,14]. Also, a growing amount of evidence indicates the importance of the poorly conserved β2-β3 loop interacting with upstream ligand residues which might play a decisive role in fine-tuning the ligand specificity [1,2,14–17].

Nuclear magnetic resonance (NMR) studies revealed that internal dynamics is an inherent property of PDZ domains. In PDZ3 of PSD-95, an extra C-terminal helix was shown to regulate ligand-dependent side-chain reorientation [16,18]. In PDZ2 of the human protein tyrosine phosphatase 1E (hPTP1E), side-chain order parameters revealed a network that triggers changes in the dynamic behavior far from the binding site [19–21].

Neighboring PDZ domains often form structural and functional supramodules termed PDZ tandems [9,22,23]. Such supramodules usually exhibit a biological function different from the simple sum of the two isolated domains. The strength and nature of the interaction between the two domains can vary on a wide range. The PDZ12 tandem of human syntenin adopts a rigid structure, and its activity is regulated by an N-terminal tail region [24,25]. Similarly, in the PDZ12 tandem of X11/Mint proteins, the C-terminal tail has an auto-inhibitory and regulatory role [26]. In turn, both PDZ12 and PDZ45 tandems of GRIP1 exhibit strong interdependence: the sole known function of one of the PDZ domains of the tandem is an intramolecular chaperoning effect, without which the other PDZ domain remains unfolded [27–29].

The supramoldular structure and dynamics of PSD-95 has been of great interest, and is suggested to be a key feature which might even influence how it selects amongst its many interaction partners [30]. However, the exact role and the mode of modulation of interdomain flexibility of its PDZ12 tandem remain elusive. The first crystal structure of PSD-95 PDZ12 tandem showed a rigid interdomain orientation with the ligands pointing to the same direction [31]. Such fixed interdomain orientation could allow for synergistic binding of membrane receptors in the postsynaptic density. Later, however, the supramodular structure of PDZ12 tandem determined by Förster resonance energy transfer (FRET) measurements indicated a different interdomain orientation in which the peptide-binding grooves pointed to the opposite direction [30,32]. Also, this study came to the conclusion that the same supramodular structure is maintained in the full-length protein as in the isolated tandem [30]. The FRET structure was subsequently refined with discrete molecular dynamic simulation and was found to be the average of many possible interdomain orientations, with two structures—an open-like and a closed-like conformation—emerging as the energetically most favorable ones [33]. This study also identified the ultraweak interdomain interactions in the two most dominant conformations that stabilize the supramodular structure of the PDZ12 tandem. Furthermore, it was shown by solution NMR experiments that the interdomain orientation is ligand dependent: the free form of

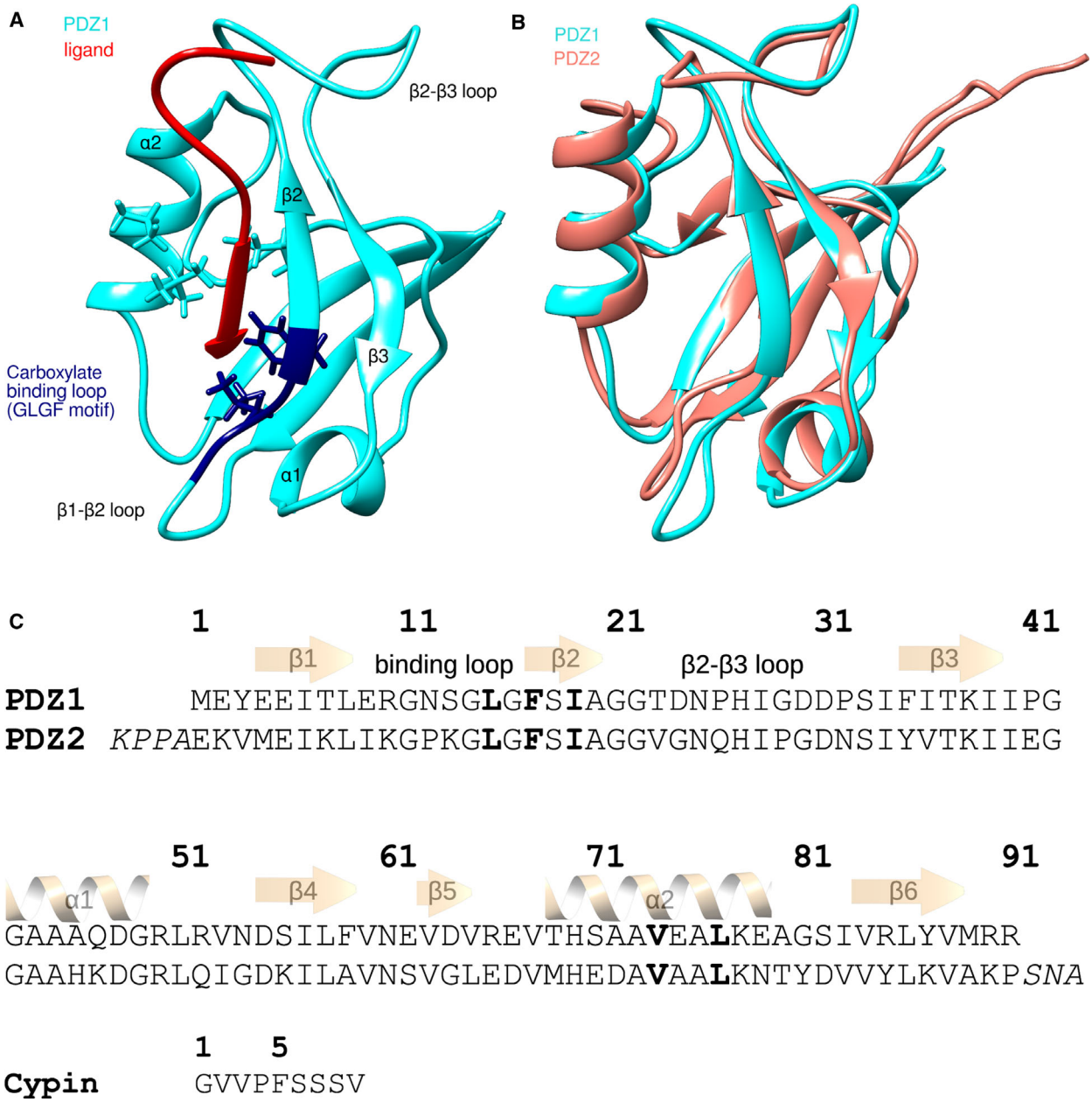

Fig. 1. The PDZ12 tandem of PSD95, taken from the PDB structure 2KA9. (A) Structure of PDZ1 bound to the 9 C-terminal residues of cypin (red). Atoms of the hydrophobic core-forming residues are explicitly shown, and the carboxylate-binding loop (GLGF motif) is colored dark blue. N and C termini are indicated. (B) Superimposed structures of PDZ1 (cyan) and PDZ2 (salmon). (C) Sequence alignment of PDZ1 and PDZ2 domains and the sequence of the ligand: 9 C-terminal residues of cypin. Residues of the carboxylate-binding loop (GLGF motif) are underlined, residues forming the hydrophobic core are highlighted in bold, whereas the linker region preceding and tail region following the PDZ2 domain is italicized.

PDZ12 tandem is rigid, whereas ligand binding induces interdomain mobility [34].

In this study, to elucidate the supramodular dynamics in the PDZ tandem and the exact atomic-level mechanism of the ligand-induced interdomain allostery, dynamic structural ensembles were generated incorporating NMR-derived distance restraints and backbone order parameters. Our results suggest interdependence of intra- and interdomain motions and provide atomic-level details of the underlying mechanism.

Methods

Generation of structural ensembles

Dynamic structural ensembles were generated with externally restrained molecular dynamics simulation. In total, three structural ensembles were created, one of the free form and two of the complex forms of PDZ12 tandem. Nuclear Overhauser effect (NOE) restraints were applied to all three ensembles, while only one of the two complex ensembles was further restrained with S^2 order parameters. Simulations were done by GROMACS 4.5.5 [38] with an in-house extension to handle NOE restraints in a pairwise manner over the replicas as well as to include S^2 order parameter restraints as described previously [39]. The first (representative) model of the solution NMR structure of PDZ12 was used as input structure which was accessed in the Protein Data Bank (PDB code: 2KA9) [34]. For the free form, the two peptide ligands (chains B and C) were manually removed.

Experimental distance restraints were downloaded from the same PDB site in v2 format. Only ^{1}H NOEs were used, in which stereospecific distance restraints were symmetrized and the resulting duplicates removed, which means 3169 ^{1}H NOEs were retained of the original 3281. Experimental backbone S^2 order parameters and chemical shifts (for N and H atoms) were kindly provided by Wenning Wang [34]. In the simulations, 79 and 80 order parameters were used for the PDZ1 and PDZ2 domains, respectively. For data validation, 170 N and H chemical shifts were used. Distance and order parameter restraints were applied in the simulations according to the MUMO protocol [40,41]. For each system, eight parallel simulations were carried out, in which NOEs were averaged in a pairwise manner, while order parameters were averaged for eight parallel replicas.

To be able to describe the independent reorientation of the two PDZ domains, the S^2 restraining routine was extended to handle local fitting for the calculation of S^2 order parameters during the simulation independently for the two domains. In this implementation, a reference frame is assigned to each S^2 parameter and the replicas are superimposed accordingly when calculating the instantaneous S^2 parameters during each simulation step. In our particular case, when calculating S^2 parameters for the first PDZ domain, the ensembles were superimposed on this domain and thus the S^2 parameters were evaluated and compared to the experimental values in order to determine restraint energies and forces independently of the orientation of the second PDZ domain.

In the simulations, covalent bonds were constrained to retain their initial bond length by the LINCS algorithm. The simulations were carried out at 300 K, in TIP3P explicit solvent model. For each system, eight parallel simulations were run for 20 ns simulation length, with 1 ps timestep. AMBER99SB-ILDN force field was applied. For temperature and pressure equilibration, the first 2000 ps of each simulation was discarded. The final simulation trajectories were sampled with 100 ps frequency, which resulted in structural ensembles with 1448 replicas for each system.

Analysis of structural ensembles

For validation of the structural ensembles, backbone RMSD values and experimental parameters were back-calculated from the ensembles. Back-calculated chemical shifts were computed with shiftx2 [42]. Chemical shifts were then ensemble-averaged over all models in each ensemble and Pearson's correlation was computed between the experimental and back-calculated chemical shifts. Back-calculated order parameters were computed with the CoNSEnsX + webserver [43]. RMSD values were calculated for backbone atoms N, Cα, and C. Both order parameters and backbone RMSD were calculated separately for the two domains, after superimposing the structures on residues 1–91 and 96–186 for the full-length PDZ1 and PDZ2 domains, respectively. Pearson's correlation coefficient for the S^2 parameters was calculated using the experimental dataset against a merged list of the values calculated independently for the two domains.

Correspondence of the generated ensembles to the experimentally determined FRET data was determined by calculating the correlation between interdomain Cα atom–atom distances and the three sets of mean interdye distances reported by Sanabria and coworkers [33]. In their work, they fit the experimentally measured ensemble time correlated single photon counting (eTCSPC) decays to three individual conformers with a three-Gaussian distributed model, thus obtaining three sets of data containing 10 mean interdomain interdye distances for each of the 10 PDZ12 tandem variant they designed. The three conformers were ranked according to population: the first, second, and third datasets belong to the most, second most, and less populated states, respectively. For calculating the correlation, the same residues were taken into account that were modified by Sanabria and coworkers and for which interdye distances were reported. The correlations are plot and shown in Fig. S11, and the individual correlations are also reported for the representative members of the resulting tight clusters as well as for all experimental structures in Table S5.

Principal component analysis (PCA) and calculation of the overlap between various PCs were carried out by ProDy [44,45]. When determining intradomain motions, due to their large and in this context functionally irrelevant fluctuations, three residues from the flexible N- and C-terminal regions were excluded from the analysis, considering only the core region of both domains: residues 4–88 (PDZ1) and 99–183 (PDZ2). When determining interdomain motions, all structures were superimposed to a common PDZ1 core region template, and PCA was carried out for the core region of PDZ2 domain, without any further displacement. Structure of the figures was created with

Chimera [46,47] and ChimeraX [47], and visual inspection of the internal motions was carried out by VMD [48].

Identifying interdomain interactions

The size of the interdomain interface was calculated as the number of heavy atom–atom contacts between the core regions of the two domains within a cutoff range of 5 Å. Structures with < 20 of such contacts were termed 'loose', while the rest were termed 'tight'. In the three structural ensembles (1448 conformers each), there were 2722 loose and 1622 tight models in total. Interdomain distance was calculated as the distance between the geometric average of all Cα atoms of the core region of the two domains.

Hydrogen bonds were identified based on angle-distance criteria [49,50]. Interdomain hydrophobic interactions were identified as close contacts (within 5 Å cutoff range) between any carbon atom in the side chain of one of the following residues: Ala, Ile, Leu, Met, Phe, Pro, Thr, Trp, Val, Arg, and Lys, or the Cα atom of Gly. The interdomain interaction forming propensity of an amino acid residue in any cluster was calculated by counting the number of interdomain contacts (separately for hydrogen bonds and hydrophobic contacts) in which the given residue is involved, and dividing it by the number of models in the given cluster. This number might rise above 1.0 if a residue is involved in more than one hydrogen bonds or hydrophobic contacts.

Calculating interdomain torsion angle

For the calculation of interdomain torsion angles, 16 data points were selected from the interdomain PCA plot (Fig. 3A,B), which are closest to 16 equidistant points lying on the best-fitting circle. Then, the best-fitting plane was determined to the centers of mass in the 3D space of the 16 different PDZ2 domain positions. In the next step, the centers of mass were projected on the 3D plane, and the center of the best-fitting circle was determined on the same plane. The 3D co-ordinates of the center of the circle in 3D space and of the normal vector of the plane (6 numbers in total) were calculated in the frame determined by the average position of Cα atoms of Phe17, Ile57, and Val84. These residues were selected for being conserved, being robust in secondary structure (part of β2, β4, and β6, respectively), and having small RMSDs. To calculate the interdomain torsion angle of any PDZ12 tandem structure, the center of the 3D circle and its normal vector is determined relative to the Cα atoms of the same three residues (Phe17, Ile57, and Val84) by using the co-ordinates obtained in the previous step.The Cα of Phe17 and the center of mass of PDZ2 domain is projected on the plane, and the interdomain torsion angle results as the angle between these two projected points relative to the center of the 3D circle (Fig. 3D).

Clustering of the ensembles

From the three generated ensembles, all tight models were selected (for details on the definition of tight models, see *Analysis of structural ensembles* in Methods). Based on the best-fitting circle fitted on the PC1 and PC2 co-ordinates of the interdomain principal components (as described in the previous section), their first and second principal components were converted into polar co-ordinates (r and θ). Using these polar co-ordinates, the tight models were clustered into 5 groups by complete linkage algorithm, and two of these clusters were further divided into 2 subclusters each. Outlier data points were removed after visual inspection. Representative structure of each cluster was identified as the one with the smallest RMSD from the average structure, computed for the backbone atoms (C, N, and Cα) of the core region of PDZ2 domain.

Results and Discussion

The generated structural ensembles correspond to the experimental data

To uncover the effect of ligand binding on the internal motions, three dynamic structural ensembles were generated with externally restrained molecular dynamic simulation of the PDZ12 tandem: one of its free state and two of its complex state. In the complex states, both PDZ domains were bound to the 9 C-terminal residues of cypin [34,35]. NOE ^{1}H-^{1}H distance restraints were applied to all the three ensembles, and one of the complex structures was further restrained with S^2 order parameters. (For the details on generating dynamic structural ensembles with NOE and S^2 restraints, see Methods).

Table 1 summarizes the RMSDs of the individual PDZ domains in all ensembles and the correlations between the experimental and back-calculated NMR parameters. Backbone RMSDs indicate that both domains in all ensembles have a well-folded, compact structure. Local RMSD values are slightly above average for the N- and C-terminal tails as well as for the β1-β2 and β2-β3 loops (Fig. S1). Since there are less experimental long-range distance restraints per residue in these regions, this difference in the local RMSD does not necessarily indicate a larger local fluctuation. Given that no explicit chemical shift restraints were used in the MD simulations, a considerable improvement in the chemical shift correlation for amide H atoms as well as some slight increase for N atoms indicates that the generated ensembles acceptably correspond to the experimental chemical shifts. Furthermore, by applying S^2 order parameters as restraints, a high correlation can be achieved without compromising chemical shift correlation (Table 1).

Table 1. Summary of the RMSD of the original and generated ensembles and their compliance with the experimental parameters. The original ensemble was accessed on the Protein Data Bank under ID 2KA9, and the rest were generated by externally restrained MD simulations (see Methods). Pearson's correlation coefficient was determined between the experimental and back-calculated parameters. RMSDs were calculated, after superimposition, for the N, C, and Cα backbone atoms in residues 1-91 (PDZ1 domain) and 96-186 (PDZ2 domain).

		Chemical shift correl.				
Ensemble	No. of conformers	N	H	S^2 correl.	PDZ1 RMSD	PDZ2 RMSD
Original PDB	20	0.83	0.41	0.10	0.57 ± 0.01	0.62 ± 0.04
Free	1448	0.85	0.55	0.22	0.73 ± 0.01	0.66 ± 0.01
Complex	1448	0.85	0.55	0.16	0.75 ± 0.02	0.58 ± 0.01
Complex (S^2 restrained)	1448	0.85	0.55	0.88	0.67 ± 0.01	0.63 ± 0.02

Dominant motions in the free form are redistributed by ligand binding in a domain-specific way

Principal component analysis (PCA) was carried out on the core region of both PDZ domains to uncover the nature of the intradomain motions (for details, see Methods). In PDZ1 domain, most of the largest principal components represent the bending of the flexible β1-β2 and β2-β3 loops, and the displacement of the α2 helix. These motions mainly differ in the direction of the relative displacement of the flexible parts. In PC1, for example, the α2 helix is moving toward and away from the β1 strand which contains the GLGF motif characteristic of PDZ domains. This motion corresponds to the opening and closing of the hydrophobic core and ligand-binding site (Fig. 2B). The binding site openness can be quantified by measuring the distance between the Cα atoms of the two hydrophobic residues LEU77 and PHE17 in PDZ1, (and, equivalently, LEU172 and PHE112 in PDZ2), located on the two opposing sites of the ligand-binding cleft, that is, in α2 and β1, respectively. These two residues accommodate the side chain of the hydrophobic C-terminal valine of the ligand.

The first principal component in PDZ1 correlates well with the binding site openness ($R = 0.78$) (Fig. 2A). The free and complex structures cover a different region along PC1 (and therefore along the binding site openness as well), with the free structures being more extended from the closed binding site almost to the widely open conformation, but the complex structures most frequently occurring in the open conformation. The binding site opening is a motion present both in the free and complex forms of PDZ1, but it is slightly quenched by ligand binding. This is also evidenced by the PC overlap plots (Fig. S9A,B), which indicate that the binding site opening is represented by the first principal component in the free form, but only by the second PC in the complex form. PC1 in the complex form, which shows a high overlap with PC2 in the whole ensemble, represents a shearing displacement of the α2 helix relative to the β1 strand, as well as the bending of the β1-β2 and β2-β3 loops. However, PC2 in the complex forms does not correlate well with the opening of the binding site ($R = 0.39$). The high overlap between PC2 in the complex ensembles and PC1 in the whole ensemble is due to the similar motion of β1-β2 and β2-β3 loops rather than to that of α2 helix, as is evidenced by PCA carried out exclusively on residues of these loops (data not shown). Despite a remarkable increase in S^2 correlation, no new internal motions in PDZ1 emerge in the S^2-restrained complex ensemble compared to the unrestrained complex one.

The PDZ2 domain, despite being structurally highly similar to PDZ1, shows some remarkable difference in its internal motions. In the first two principal components, the bending of the β1-β2 and β2-β3 loops is dominant, and the α2 helix is but very slightly displaced (Fig. 2D). This results in a low correlation between PC1 or PC2 and the binding site openness ($R = 0.41$). By excluding the flexible loops (residues 105-109 and 117-127) from the PCA, a slightly better correlation can be achieved ($R = -0.47$), which is even higher for the free structures only ($R = -0.50$). However, by plotting PC1 of the truncated PDZ2 structure against the binding site openness, the free and the complex structures show some slight separation along both axes (Fig. 2C). The effect, therefore, that the binding of the ligand quenches the binding site opening is still present in PDZ2, but is far less pronounced than in PDZ1. The overlap between the internal motions of the whole ensemble and those of the free and complex states (Fig. S9C,D) also conform this observation.

Interdomain motions: the relative orientation of the two domains covers a large conformational space

In order to investigate the interdomain mobility, the PDZ1 domains in all three ensembles were

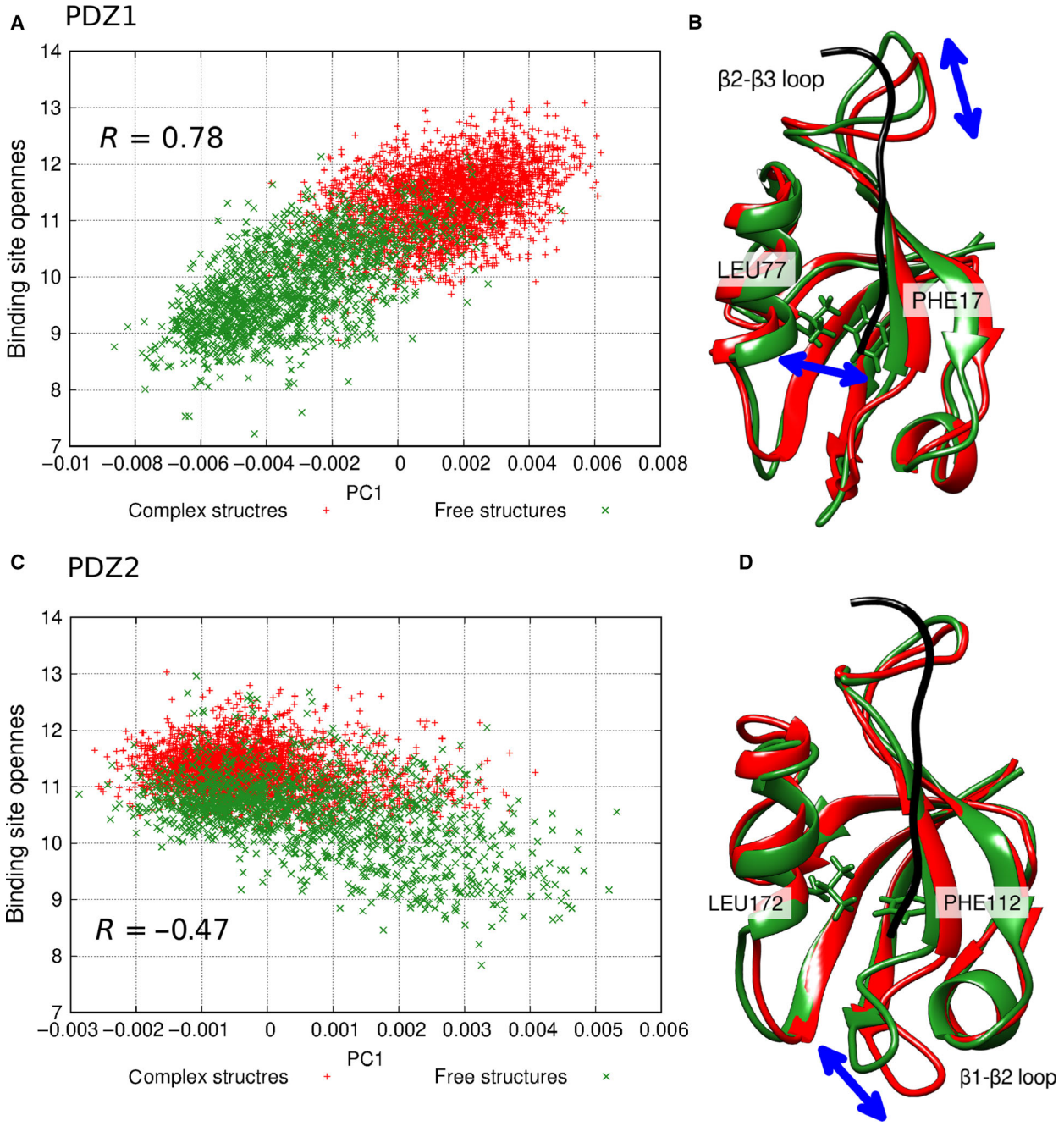

Fig. 2. Intradomain motions in PDZ1 (A, B) and PDZ2 (C, D) domains. (A, C) Binding site openness (i.e., distance between Cα of PHE17-LEU77 and PHE112-LEU172 in PDZ1 and PDZ2, respectively), plotted against the first principal component (PC1). PC1 for PDZ2 domain in this plot was calculated for the truncated structure (for details, see text). (B, D) Ribbon representation of PC1 in PDZ1 and PDZ2 domains, the most mobile regions are indicated with blue arrow. Red and green colors represent the displacement in the fluctuations along PC1 relative to the mean structure: the green and red colors are more populated in the free and complex states, respectively.

superimposed to a common template. This results in a very well-aligned PDZ1 domain (RMSD = 0.81), whereas the PDZ2 domain samples a large number of different orientations (RMSD = 22.93), highlighting the relative displacement between the two domains. Using these superimposed ensembles, principal component analysis (PCA) was carried out only on the orientations of the core regions of PDZ2 domain relative to

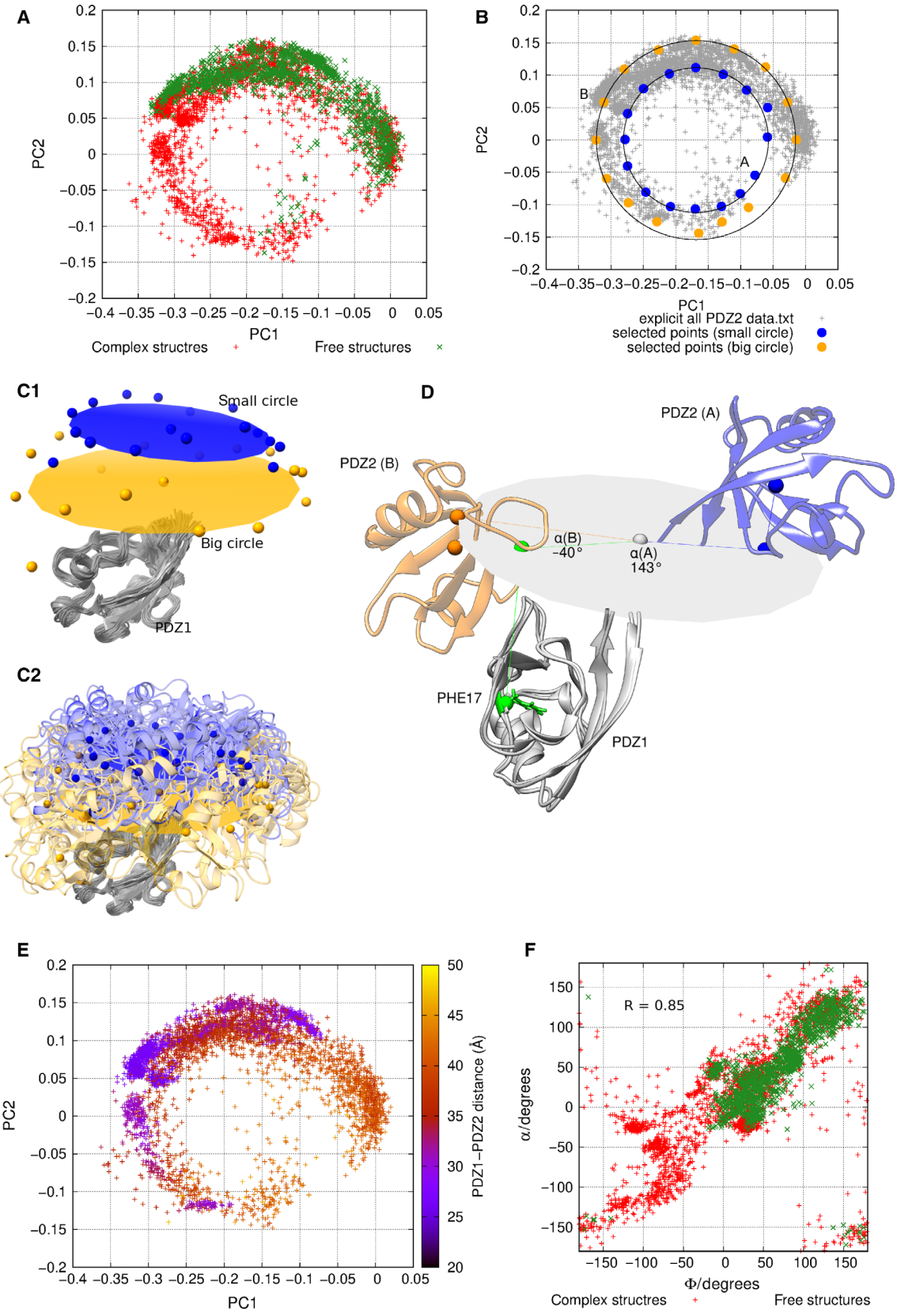

Fig. 3. Interdomain motions. (A) PCA plot of the displacement of PDZ2 domain relative to PDZ1. (B) Two circles fitted to the interdomain PCA plot (with radii 0.8 and 1.1 times of that of the best-fitting circle) 2 × 16 data points are highlighted, which are closest to the 16 equidistant points on each circle. (C1, C2) The centers of mass of the PDZ2 domain in different orientations relative to PDZ1. (D) Illustration of the interdomain torsion angle (α) in two selected interdomain orientations (also indicated on B). For description, see Methods. (E) PCA plot of the interdomain motions, with color-coded distance between the centers of masses of PDZ1 and PDZ2 domains. (F) Interdomain torsion angle calculated as presented above (α) plotted against the interdomain torsion angle calculated as described by Zhang and coworkers (Φ) [34].

PDZ1 (for details, see Methods). The first and second principal components cover 48% and 32% of the variability of the structures, respectively.

When plotting the resulting first and second principal components, the data points exhibit a circular arrangement (Fig. 3A). The data points were sampled along two circles that have a radius 0.8 and 1.1 times that of the best-fitting circle in a way that the nearest data point was chosen to the 16 equidistant points in both circles (Fig. 3B). Upon visual inspection, it became evident that these data points, which lie along a 2D circle on the PCA plot, represent such PDZ-tandem structures where the PDZ2 domains are arranged along a 3D circle (with the PDZ1 domains being superimposed). Furthermore, the distance of each data point from the center of the circle corresponds to the degree by which the orientation of the two domains deviates from the extended interdomain conformation, that is, the interdomain bending angle. This observation can be best demonstrated by plotting the centers of mass of the PDZ2 domains that were sampled from the two circles: they fit relatively well to two nearly parallel circles (Fig. 3C).

Taking advantage of the exhaustively sampled interdomain conformational space, an interdomain torsion angle (denoted by α) can easily be defined (Fig. 3D, for details, see Methods). The angle component of the polar co-ordinates calculated from the first and second principal components, after phase correction, correlate extremely well with the interdomain torsion angle ($R = 0.98$) and also with the interdomain torsion angle defined by Zhang *et al.* [34] (Fig. 3F, denoted as ϕ) ($R = 0.85$).

The presence of the ligand has a remarkable effect on the covered interdomain conformational space: in the complex form, the whole circle is relatively well sampled, whereas in the ligand-free form only a part of the full circle is covered (Fig. 3A). The same effect is also evident from the interdomain torsion angles: the complex form allows for much more extended interdomain motions (Fig. 3F). This observation is in accordance with the fact that a dynamic equilibrium in the interdomain interface is built up more slowly when the ligand is present (Fig. S6).

Strikingly, the position of the superimposed PDZ1 domain relative to the circle along which PDZ2 domain moves is not perfectly centered, but slightly tilted toward one side (Fig. 3C). This results in a thinly sampled region in the interdomain PCA plot, but—more importantly— a shorter interdomain distance and, consequently, more interdomain contacts on one side of the sampled circle (Fig. 3E).

Structures forming an interdomain interface can be clustered according to the interdomain orientation

A shorter interdomain distance allows for more interdomain contacts (Fig. 3E). Structures in which there were at least 20 interdomain atom–atom contacts between heavy atoms within a 5 Å cutoff range (termed 'tight structures') occupy only a fraction of the whole interdomain conformational space (Fig. S5). The ratio of the tight interdomain conformers in the free and complex ensembles resulted to be 32% and 40%, respectively. Using the polar co-ordinates, computed with the aid of the best-fitting circle (Fig. 3B), the tight structures can be clustered in seven clusters by hierarchical clustering algorithm (complete linkage) (Fig. 4A). (For details on clustering the ensembles, see Methods). The seven representative structures correspond to seven tightly packed interdomain orientations, in which the interdomain interface is formed between different regions (Fig. 4B). For better visibility, the surface of the PDZ domain was divided into five sites and termed head, tail, back, left side, and right side, relative to the ligand-binding site (Fig. 4C, Fig. S3). Figure 4E summarizes the interface-forming sites in PDZ1 and PDZ2 domains, as well as the alignment of the two ligands. Compared to the raw ensembles, no significant changes can be observed in the chemical shift correlation computed for the clusters, which indicates that chemical shift correlations are robust in the selected subensembles (Table S2). For more details on the clusters, see Table S1.

The orientation of the 4 C-terminal residues of the ligand depends on the interdomain torsional angle, and therefore it also differs from cluster to cluster.

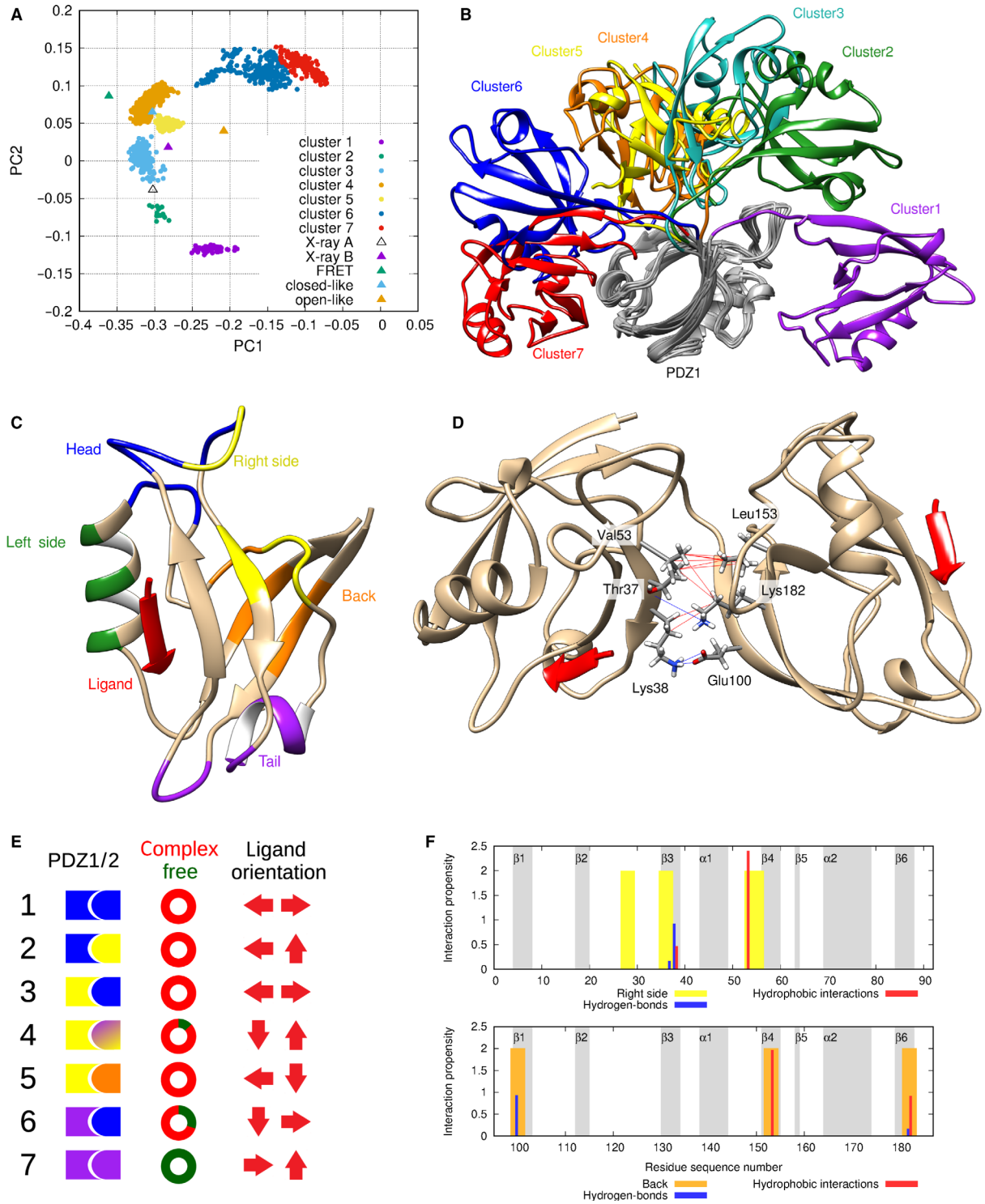

Fig. 4. Interdomain clusters. (A) Plot of interdomain PC1 and PC2 of the clusters created from structures with tight interdomain interface. Experimental structures are included (FRET, open-like, and closed-like are kindly provided by Mark Bowen) [33], and X-ray structures were downloaded from PDB (ID: 3GLS) [36]. (B) Representative structure of each cluster. (C) Interface-forming sites in PDZ domain. (D) Representative structure of cluster 5. (E) Summary of the interdomain interface (first column), the complex to free form ratio (second column), and the ligand alignment (third column). (F) Interdomain interaction (hydrogen bonds and hydrophobic interaction, highlighted with blue and red, respectively) forming propensities of the residues in both domains, as found in cluster 5 (for interaction forming propensity, see Methods).

The C-terminal tail of the ligand, pointing in the same direction, facilitates synergistic binding of the membrane receptors in the postsynaptic density, suggested and discussed by Zhang *et al.* [31]. However, in none of the tight orientations represented by these clusters are the two ligands orientated parallel to each other and in the same time perpendicular to the interdomain axis, the arrangement which could allow for such synergistic binding. In many clusters, the perpendicular or antiparallel ligand orientation could allow one PDZ domain to bind a membrane receptor, and the other one to bind an intracellular partner. Nonetheless, it is not to be forgotten that all members of the clusters are composed of tight PDZ12 tandems, which only cover a fraction of the interdomain conformational space. Considering all the possible interdomain conformations, in which the two domains are not necessarily in interaction, there are many in which the ligands are in parallel orientation (Fig. S4).

Resulting from the interface-forming sites, the main interactions, which hold the two domains together, also differ from cluster to cluster. All interdomain hydrogen bonds as well as hydrophobic interactions were determined in each conformation (for details, see Methods). Those interactions that are present in at least 10% of the conformations in any cluster are listed in Table S3. For demonstration, the representative structure of cluster 5 and the residues involved in interdomain hydrogen bonds or hydrophobic interactions are shown in Fig. 4D,F. Figure 4F also shows that the interacting residues fall well within the previously defined interface-forming sites. The interdomain interface and the ligand orientation in the rest of the clusters are shown in Fig. S7.

PDZ12 tandem structures of PSD-95 determined previously by various experimental techniques were checked and compared to our clusters (Fig. 4A, Fig. S10). These experimental structures include, in particular, two chains of the same crystal structure from PDB (ID: 3GSL) [36], a structure determined by FRET presented by Bowen *et al.* [30], and two further structures, an open-like and a closed-like conformation, resulting from the refinement of the same FRET structure by DMD simulations and presented by Sanabria and coworkers [33] (5 structures in total).

Both X-ray structures are lying on the edge of cluster 3 on the PCA plot, and they also form an interdomain interface between the right side of PDZ1 and the head of PDZ2, which is characteristic of cluster 3 (see Fig. 4C). The fact that both X-ray structures of the PDZ12 tandem are to be found within the conformational space covered by tight conformers is in agreement with the expectation that in crystallized state the two domains should be closely packed and therefore form a large interdomain interface.

The FRET structure falls outside of the circle of the interdomain conformational space covered by our simulations. However, reanalysis of the structure revealed that it represents the average of two states, an open- and a closed-like conformation [33]. The corresponding refined structures are covered by the conformational space explored in this study. The open-like, as can be expected, does not belong to any cluster, since it does not contain enough close interdomain atom–atom contacts to be part of the tight models.The closed-like conformation, on the other hand, lies at the edge of cluster 4, and, indeed, forms the interdomain interface between the sites termed 'right side' in both domains. It should be noted that were the two domains closer to one another in the open-like conformation, their relative orientation would allow for a larger interdomain interface between the right side of PDZ1 and the head of PDZ2, which would make it a member of cluster 3, rather than cluster 4 or 5, to which it is closer on the PCA plot.

To further analyze the correspondence between our simulations and the experimentally determined structures, the correlation was calculated between our structures and the data resulting from FRET measurements presented by Sanabria and coworkers [33] (Fig. S11 and Table S5) (for details, see Methods). In the work of Sanabria *et al.*, 3 sets of 10 interdye distances are reported, each belonging to a supertertiary conformational state. The most and second most populated of these two states were identified as the open-like and the closed-like conformations, respectively, whereas the third was concluded to be the average of a larger pool of conformations. It is important to note that a correlation near 1.0 cannot be expected since the experimental data fit the interdye distance, whereas in our calculations Cα atom–atom distances were used.

The regions correlating best with the first, second, and third interdye distance datasets are relatively well separated on the PCA plot (Fig. S11). Based on our findings, the relationship between the two most populated states and the open- and closed-like conformations can be confirmed (Table S5). Furthermore, the correlations also confirm that the closed-like confirmation belongs to cluster 4, whereas for the open-like, while showing relatively good correlation with a number of clusters, no clear cluster membership can be attributed. Interestingly, the third dataset, while showing generally lower correlations with all clusters, clearly belongs to cluster 7, but the area where the correlations are highest extends well into the region of the

loose conformers. In conclusion, the three conformational states resulting from the experimental FRET measurements [33] correlate well with the conformational space explored in our MD simulations.

Intra- and interdomain motions are interdependent

We analyzed the interdependence of intra- and interdomain motions. By plotting the principal components of intradomain motions and coloring each dot (representing a structure) according to the cluster of interdomain arrangement it belongs to, it is observed that intradomain conformations and interdomain orientations are not completely independent (Fig. S8). It should be noted that the clusters contain both complexed and ligand-free structures. Furthermore, in PDZ2, clusters 1 and 7 are both slightly separated from the rest, even though complex forms are represented in a very high and low ratio in them, respectively.

As it was shown earlier, in PDZ1, the first principal component represents both the opening and closing of the binding site as well as the bending of β1-β2 and β2-β3 loops. In contrast, the binding site opening is suppressed by the bending of the β1-β2 loop in PDZ2. By comparing these regions to the sites introduced to define the interdomain interfaces, it is clear that β1-β2 constitutes the tail site while β2-β3 loop is involved in both the head region and right side (Fig. S3). By looking at Fig. 4E, one can clearly see that in all but one clusters, at least one of these sites (i.e., the head or right side in PDZ1 or the tail in PDZ2) is involved in the interdomain interface.

Even though PDZ domains are traditionally categorized according to only the 4 C-terminal residues of their binding partner, the role of the upstream residues of the ligand has been emphasized recently [2]. To gain further insight into the interaction between the PDZ domains and the ligand, hydrogen bonds were identified between both PDZ domains and the simulated cypin ligand, and their occurrences were calculated in percentages in all 7 clusters (Table S4). Apart from 3 hydrogen bonds present in high percentage in all clusters (between residues 0 and −2 in the ligand, and β2 strand in the PDZ domain), the rest of the bonds—many of them being formed between upstream ligand residues and the β2-β3 loop—show a different pattern in different clusters. This indicates a fine-tuned regulative interaction between ligand binding, intradomain dynamics, and interdomain orientation. This finding is in accordance with the previously suggested regulative role of the β2-β3 loop in binding specificity [2,16].

Based on the above-presented results, it is convenient to assume that interdomain orientation and the bound ligand are fine-tuning and regulating each other through a number of weak, atomic-level interactions. This might, in part, explain how the N-terminal PDZ domains of PSD-95 are capable of binding multimeric membrane-associated ligands as well as intracellular signaling proteins at the same time. This idea might fit well into the picture presented by Bowen and coworkers [32], according to which the PDZ12 tandem within the PSD-95 protein forms an independent conformational unit and is capable of performing detached motions from the other parts of the protein.

Conclusions

The PSD-95 protein in the postsynaptic density of nerve cells performs numerous biological functions that require its peptide-binding PDZ domains to be able to form versatile interactions with a number of binding partners. However, it is still unclear how PSD-95 discriminates between its ligands [30]. The PDZ12 tandem of PSD-95 was shown to exhibit different function from the simple sum of the two constituting domains [22,31,37], but the exact atomic-level interactions between the two domains and the extent of interdomain reorientation remain elusive.

In this study, dynamic structural ensembles of the ligand-free and complexed forms of the PDZ12 tandem were created by externally restrained molecular dynamics simulations. ^{1}H-^{1}H NOEs were applied as distance restraints in both forms, and an additional ensemble was created of the complexed form in which S^2 order parameter restraints were also incorporated. Applying the S^2 restraints separately on each domain does not largely influence the interdomain conformational space, but it yields a description of the intradomain motions which is consistent with the experimental S^2 parameters. Thus, we are capable of obtaining a description of possible interdomain orientations while keeping fast intradomain motions consistent with experimental observations. It is important to stress that no explicit restraining or other explicit influencing of interdomain interactions and orientation is present in our calculations. Restraining by S^2 order parameters, representing motions on the fast ps–ns regime, is applied on the domains separately, allowing their independent, plausibly slower relative reorientation.

Our ensembles descriptive of the intra- and interdomain motions are in agreement with previous experimental findings, that is, ligand binding changes the dynamics of the β2-β3 loop and considerably expands

the interdomain conformational space as well. The structural ensembles presented in this study provide a dynamic interpretation of the supramodular structural rearrangement of the PDZ12 tandem upon ligand binding. Our analysis is relevant in terms of the dynamics of the formation of the ligand-bound form and gives an estimation on the redistribution of possible interdomain orientations of the PDZ12 tandem upon ligand binding and release.

The formation of the interdomain interface is not independent from the ligand binding. Our most important finding is that the different possible interdomain orientations, necessary to form certain interdomain interfaces, are influenced by the intradomain motions, or more specifically, by motions of the flexible and poorly conserved β2-β3 and β1-β2 loops in PDZ1, and of the β1-β2 loop in PDZ2 domain. The β2-β3 loop has already been suggested to play a key role in discriminating between different binding partners of PDZ domains [2], which is consistent with our analysis where we show that this loop is one of the regions that is most prone to forming interdomain interactions.

One has to be careful when interpreting these results in terms of *in vivo* behavior of the PDZ12 tandem of PSD-95. Our simulations included short peptide ligands for the PDZ12 tandem, whereas its actual binding partners are large proteins, which might induce a steric constraint on the possible interdomain orientations. On the other hand, amongst the binding partners of PSD-95 there are membrane proteins as well as intracellular proteins [10], many of which are bound by one or more PDZ domains. In theory, multiple binding partners might orient toward the PSD-95 scaffold protein from different sites. Furthermore, PDZ12 tandem was shown to form an independent conformational subunit within PSD-95, which is guaranteed by the ~ 60-residue long linker that connects the PDZ12 tandem to PDZ3 and the rest of the protein [32]. This gives enough reason to speculate that supramodular flexibility is an inherent property not only of PSD-95 but its PDZ12 tandem as well, and its dynamics is necessary to perform the proper biological function.

In summary, our results strongly suggest that ligand binding regulates interdomain orientation by modulating the probabilities of the formation of domain–domain interactions through different interdomain interfaces. It is also worth speculating that, vice versa, the relative orientation of the two domains in the PDZ12 tandem might have a role in shifting the preference for different binding partners, with the aid of the same β2-β3 loop. Additional—both *in vitro* and silico—investigation of the ligand-dependent interdomain dynamics of PDZ12 tandem of PSD-95 may shed light on its supramodular nature and help us further understand the molecular mechanisms behind the PSD-95 modulated rearrangement of the postsynaptic density in neuron cells.

Acknowledgments

The authors acknowledge the support of the National Research, Development and Innovation Office (NKFIH) through grant nos NF104198 and NN124363. Z.G. has been supported by a János Bolyai Research fellowship from the Hungarian Academy of Sciences. The research has been supported by the European Union and cofinanced by the European Social Fund (EFOP-3.6.2-16-2017-00013, Thematic Fundamental Research Collaborations Grounding Innovation in Informatics and Infocommunications).

Author contributions

BK ran the simulations, carried out the data analysis and prepared the manuscript. NZ-E implemented the fitting algorithm for local S^2 order parameter restraining. ZG designed and supervised the study.

Note added in proof

Just before the acceptance of our paper, a preprint has been posted on bioRxiv (Rodzli et al.: How the dual PDZ domain from Postsynaptic density protein 95 clusters ion channels and receptors, https://doi.org/10.1101/775726) that describes two structures of the PDZ12 tandem. These structures, available in the Protein Data Bank with the IDs 6spv and 6spz, fit well into our cluster 6 (Fig. 4A), lending experimental support for the diversity of interdomain orientations proposed based on our simulations.

References

1 Ernst A, Appleton BA, Ivarsson Y, Zhang Y, Gfeller D, Wiesmann C and Sidhu SS (2014) A structural portrait of the PDZ domain family. *J Mol Biol* **426**, 3509–3519.
2 Luck K, Charbonnier S and Travé G (2012) The emerging contribution of sequence context to the specificity of protein interactions mediated by PDZ domains. *FEBS Lett* **586**, 2648–2661.
3 Fanning AS and Anderson JM (1999) PDZ domains: fundamental building blocks in the organization of protein complexes at the plasma membrane. *J Clin Invest* **103**, 767–772.
4 Harris BZ and Lim WA (2001) Mechanism and role of PDZ domains in signaling complex assembly. *J Cell Sci* **114**, 3219–3231.

5 Hung AY and Sheng M (2002) PDZ domains: structural modules for protein complex assembly. *J Biol Chem* **277**, 5699–5702.

6 Nourry C, Grant SGN and Borg J (2003) PDZ Domain Proteins: Plug and Play!. *Sci Signal* **2003**, re7

7 Sheng M and Sala C (2001) PDZ domains and the organization of supramolecular complexes. *Annu Rev Neurosci* **24**, 1–29.

8 Craven & Bredt (1998) PDZ proteins organize synaptic signaling pathways. *Cell* **93**, 495–498.

9 Feng W and Zhang M (2009) Organization and dynamics of PDZ-domain-related supramodules in the postsynaptic density. *Nat Rev Neurosci* **10**, 87–99.

10 Kim E and Sheng M (2004) PDZ domain proteins of synapses. *Nat Rev Neurosci* **5**, 771–781.

11 Gardoni F, Marcello E and Di Luca M (2009) Postsynaptic density-membrane associated guanylate kinase proteins (PSD-MAGUKs) and their role in CNS disorders. *Neuroscience* **158**, 324–333.

12 Doyle DA, Lee A, Lewis J, Kim E, Sheng M and MacKinnon R (1996) Crystal structures of a complexed and peptide-free membrane protein- binding domain: molecular basis of peptide recognition by PDZ. *Cell* **85**, 1067–1076.

13 Morais Cabral JH, Petosa C, Sutcliffe MJ, Raza S, Byron O, Poy F, Marfatia SM, Chishti AH and Liddington RC (1996) Crystal structure of a PDZ domain. *Nature* **382**, 649–52.

14 Tonikian R, Zhang Y, Sazinsky SL, Currell B, Yeh JH, Reva B, Held HA, Appleton BA, Evangelista M, Wu Y, et al (2008) A specificity map for the PDZ domain family. *PLoS Biol* **6**, 2043–2059.

15 Imamura F, Maeda S, Doi T and Fujiyoshi Y (2002) Ligand binding of the second PDZ domain regulates clustering of PSD-95 with the Kv1.4 potassium channel. *J Biol Chem* **277**, 3640–3646.

16 Mostarda S, Gfeller D and Rao F (2012) Beyond the binding site: the role of the β2 – β3 loop and extra-domain structures in PDZ domains. *PLoS Comput Biol* **8**, e1002429.

17 Tochio H, Hung F, Li M, Bredt DS and Zhang M (2000) Solution structure and backbone dynamics of the second PDZ domain of postsynaptic density-95. *J Mol Biol* **295**, 225–37.

18 Petit CM, Zhang J, Sapienza PJ, Fuentes EJ and Lee AL (2009) Hidden dynamic allostery in a PDZ domain. *Proc Natl Acad Sci USA* **106**, 18249–18254.

19 Dhulesia A, Gsponer J and Vendruscolo M (2008) Mapping of two networks of residues that exhibit structural and dynamical changes upon binding in a PDZ domain protein. *J Am Chem Soc* **130**, 8931–8939.

20 Fuentes EJ, Der CJ and Lee AL (2004) Ligand-dependent Dynamics and Intramolecular Signaling in a PDZ Domain. *J Mol Biol* **335**, 1105–1115.

21 Fuentes EJ, Gilmore SA, Mauldin RV and Lee AL (2006) Evaluation of energetic and dynamic coupling networks in a PDZ domain protein. *J Mol Biol* **364**, 337–351.

22 Wang CK, Pan L, Chen J and Zhang M (2010) Extensions of PDZ domains as important structural and functional elements. *Protein Cell* **1**, 737–751.

23 Ye F and Zhang M (2013) Structures and target recognition modes of PDZ domains: recurring themes and emerging pictures. *Biochem J* **455**, 1–14.

24 Cierpicki T, Bushweller JH and Derewenda ZS (2005) Probing the supramodular architecture of a multidomain protein: the structure of syntenin in solution. *Structure* **13**, 319–327.

25 Kang BS, Cooper DR, Jelen F, Devedjiev Y, Derewenda U, Dauter Z, Otlewski J and Derewenda ZS (2003) PDZ tandem of human syntenin: Crystal structure and functional properties. *Structure* **11**, 459–468.

26 Long J-F, Feng W, Wang R, Chan L-N, Ip FCF, Xia J, Ip NY and Zhang M (2005) Autoinhibition of X11/Mint scaffold proteins revealed by the closed conformation of the PDZ tandem. *Nat Struct Mol Biol* **12**, 722–728.

27 Feng W, Shi Y, Li M and Zhang M (2003) Tandem PDZ repeats in glutamate receptor-interacting proteins have a novel mode of PDZ domain-mediated target binding. *Nat Struct Biol* **10**, 972–978.

28 Long J, Wei Z, Feng W, Yu C, Zhao YX and Zhang M (2008) Supramodular nature of GRIP1 revealed by the structure of its PDZ12 tandem in complex with the carboxyl tail of Fras1. *J Mol Biol* **375**, 1457–1468.

29 Zhang Q, Fan JS and Zhang M (2001) Interdomain chaperoning between PSD-95, Dlg, and Zo-1 (PDZ) domains of glutamate receptor-interacting proteins. *J Biol Chem* **276**, 43216–43220.

30 McCann JJJ, Zheng L, Chiantia S and Bowen MEE (2011) Domain orientation in the N-terminal PDZ tandem from PSD-95 is maintained in the full-length protein. *Structure* **19**, 810–820.

31 Long JF, Tochio H, Wang P, Fan JS, Sala C, Niethammer M, Sheng M and Zhang M (2003) Supramodular structure and synergistic target binding of the N-terminal tandem PDZ domains of PSD-95. *J Mol Biol* **327**, 203–214.

32 McCann JJ, Zheng L, Rohrbeck D, Felekyan S, Kuhnemuth R, Sutton RB, Seidel CAM and Bowen ME (2012) Supertertiary structure of the synaptic MAGuK scaffold proteins is conserved. *Proc Natl Acad Sci USA* **109**, 15775–15780.

33 Yanez Orozco IS, Mindlin FA, Ma J, Wang B, Levesque B, Spencer M, Rezaei Adariani S, Hamilton G, Ding F, Bowen ME and et al (2018) Identifying weak interdomain interactions that

stabilize the supertertiary structure of the N-terminal tandem PDZ domains of PSD-95. *Nat Commun* **9**, 3724.
34 Wang W, Weng J, Zhang X, Liu M and Zhang M (2009) Creating conformational entropy by increasing interdomain mobility in ligand binding regulation: a revisit to N-terminal tandem PDZ domains of PSD-95. *J Am Chem Soc* **131**, 787–796.
35 Firestein BL, Firestein BL, Brenman JE, Aoki C, Sanchez-Perez AM, El-Husseini AE and Bredt DS (1999) Cypin: a cytosolic regulator of PSD-95 postsynaptic targeting. *Neuron* **24**, 659–672.
36 Sainlos M, Tigaret C, Poujol C, Olivier NB, Bard L, Breillat C, Thiolon K, Choquet D and Imperiali B (2010) Biomimetic divalent ligands for the acute disruption of synaptic AMPAR stabilization. *Nat Chem Biol* **7**, 81.
37 Bach A, Clausen BH, Møller M, Vestergaard B, Chi CN, Round A, Sørensen PL, Nissen KB, Kastrup JS, Gajhede M, et al (2012) A high-affinity, dimeric inhibitor of PSD-95 bivalently interacts with PDZ1-2 and protects against ischemic brain damage. *Proc Natl Acad Sci USA* **109**, 3317–3322.
38 Hess B, Kutzner C, Van Der Spoel D and Lindahl E (2008) GRGMACS 4: algorithms for highly efficient, load-balanced, and scalable molecular simulation. *J Chem Theory Comput* **4**, 435–447.
39 Fizil Á, Gáspári Z, Barna T, Marx F and Batta G (2015) "Invisible" conformers of an antifungal disulfide protein revealed by constrained cold and heat unfolding, CEST-NMR experiments, and molecular dynamics calculations. *Chemistry* **21**, 5136–5144.
40 Best RB and Vendruscolo M (2004) Determination of protein structures consistent with NMR order parameters. *J Am Chem Soc* **126**, 8090–8091.
41 Richter B, Gsponer J, Vérnai P, Salvatella X, Vendruscolo M, Várnai P, Salvatella X and Vendruscolo M (2007) The MUMO (minimal under-restraining minimal over-restraining) method for the determination of native state ensembles of proteins. *J Biomol NMR* **37**, 117–135.
42 Han B, Liu Y, Ginzinger SW and Wishart DS (2011) SHIFTX2: significantly improved protein chemical shift prediction. *J Biomol NMR* **50**, 43–57.
43 Dudola D, Kovács B and Gáspári Z (2017) CoNSEnsX + Webserver for the analysis of protein structural ensembles reflecting experimentally determined internal dynamics. *J Chem Inf Model* **57**, 1728–1734.
44 Bakan A, Meireles LM and Bahar I (2011) ProDy: protein dynamics inferred from theory and experiments. *Bioinformatics* **27**, 1575–1577.
45 Bakan A, Dutta A, Mao W, Liu Y, Chennubhotla C, Lezon TR and Bahar I (2014) Evol and ProDy for bridging protein sequence evolution and structural dynamics. *Bioinformatics* **30**, 2681–2683.
46 Pettersen EF, Goddard TD, Huang CC, Couch GS, Greenblatt DM, Meng EC and Ferrin TE (2004) UCSF Chimera–a visualization system for exploratory research and analysis. *J Comput Chem* **25**, 1605–1612.
47 Goddard TD, Huang CC, Meng EC, Pettersen EF, Couch GS, Morris JH and Ferrin TE (2018) UCSF ChimeraX: meeting modern challenges in visualization and analysis. *Protein Sci* **27**, 14–25.
48 Humphrey W, Dalke A and Schulten K (1996) VMD: visual molecular dynamics. *J Mol Graph* **14**, 33–38.
49 Baker EN and Hubbard RE (1984) Hydrogen bonding in globular proteins. *Prog Biophys Mol Biol* **44**, 97–179.
50 Xu D, Tsai C-J and Nussinov R (1997) Hydrogen bonds and salt bridges across protein-protein interfaces. *Protein Eng Des Sel* **10**, 999–1012.

Supporting information

Additional supporting information may be found online in the Supporting Information section at the end of the article.

Figure S1. Local RMSDs of the original and generated ensembles (top) and the number of long-range NOE distance restraints per residue (bottom).
Figure S2. Plots of the experimental (purple) and back-calculated (green) S2 order parameters vs. the residue sequence numbers.
Figure S3. Sites in PDZ1 and PDZ2 domains.
Figure S4. Distribution of the structures in the interdomain conformational space according to ligand orientation.
Figure S5. Distribution of 'loose' and 'tight' PDZ12 tandem structures in the interdomain conformational space.
Figure S6. Evolution of the interdomain interface in time as observed along the simulation trajectories.
Figure S7. Supplementary figures about each cluster.
Figure S8. Separation of the tight clusters along intradomain motional modes, for PDZ1 and PDZ2 domains.
Figure S9. Overlap between the first 4 principal components of different ensembles.
Figure S10. Structures of PSD-95 PDZ12 tandem determined by various experimental methods.
Figure S11. Correlation of the generated ensembles to FRET data presented in Yanez Orozco et al., 2018.

Table S1. The 7 clusters created from the tight models, their size and composition, their interdomain interface, and the orientation and location of the ligand.

Table S2. RMSDs and correspondence between the experimental and back-calculated parameters, derived from the 7 clusters.

Table S3. Occurrences of interdomain hydrogen bonds and hydrophobic interactions, with the two interacting atoms specified (rows) in every cluster (columns).

Table S4. Hydrogen bonds between the domains and the ligands.

Table S5. Correlations between individual structures (representative structures of the clusters, extracted from the MD simulations as well as experimental structures) and the experimental FRET data, reported in Yanez Orozco et al., 2018.